Nanoscale

PAPER

View Article Online
View Journal | View Issue

Cite this: *Nanoscale*, 2021, **13**, 311

Tailored synthesis approach of $(Mo_{2/3}Y_{1/3})_2AlC$ *i*-MAX and its two-dimensional derivative $Mo_{1.33}CT_z$ MXene: enhancing the yield, quality, and performance in supercapacitor applications†

Joseph Halim, *[a] Ahmed S. Etman, [a] Anna Elsukova,[a] Peter Polcik,[b] Justinas Palisaitis, [a] Michel W. Barsoum, [a,c] Per O. Å. Persson [a] and Johanna Rosen *[a]

A vacancy-ordered MXene, $Mo_{1.33}CT_z$, obtained from the selective etching of Al and Sc from the parent *i*-MAX phase $(Mo_{2/3}Sc_{1/3})_2AlC$ has previously shown excellent properties for supercapacitor applications. Attempts to synthesize the same MXene from another precursor, $(Mo_{2/3}Y_{1/3})_2AlC$, have not been able to match its forerunner. Herein, we show that the use of an $AlY_{2.3}$ alloy instead of elemental Al and Y for the synthesis of $(Mo_{2/3}Y_{1/3})_2AlC$ *i*-MAX, results in a close to 70% increase in sample purity due to the suppression of the main secondary phase, Mo_3Al_2C. Furthermore, through a modified etching procedure, we obtain a $Mo_{1.33}CT_z$ MXene of high structural quality and improve the yield by a factor of 6 compared to our previous efforts. Free-standing films show high volumetric (1308 F cm^{-3}) and gravimetric (436 F g^{-1}) capacitances and a high stability (98% retention) at the level of, or even beyond, those reported for the $Mo_{1.33}CT_z$ MXene produced from the Sc-based *i*-MAX. These results are of importance for the realization of high quality MXenes through use of more abundant elements (Y *vs.* Sc), while also reducing waste (impurity) material and facilitating the synthesis of a high-performance material for applications.

Received 1st October 2020,
Accepted 1st December 2020

DOI: 10.1039/d0nr07045a

rsc.li/nanoscale

1. Introduction

Two-dimensional (2D) materials comprise a huge variety of both compositions and structures, translating into great potential for various applications.[1–5] Since 2011, the atomically layered ternary transition metal carbides and/or nitrides known as MAX phases have gained increased attention from the scientific community, as they serve as precursor for their 2D derivative, the family of so called MXenes.[6–8] MAX phases display a hexagonal crystal structure and are described by the general formula $M_{n+1}AX_n$, where M stands for an early transition metal (*e.g.* Ti, Mo, V, Nb), A stands for mostly a group 13 or 14 element, and X stands for carbon and/or nitrogen; n = 1–4.[6] This family exhibits both ceramic and metallic properties, including high electrical and thermal conductivities,[9,10] machinability and damage tolerance.[11] Some are also lightweight,[12] oxidation resistant, self-healing,[12] and maintain their strengths at high temperatures.[11] Some are magnetic.[13,14]

Their 2D counterparts, MXenes, are 2D transition metal carbides and/or nitrides produced by selective etching of the A element, typically Al, from the MAX phases.[15] MXenes have the general formula $M_{n+1}X_nT_z$, where T stands for surface terminating groups (–O, –OH, –F and/or –Cl)[16–19] that replaces the A layer upon etching. To date, MXenes have shown promise for a wide range of applications, including energy storage,[20,21] hydrogen evolution,[22–24] photocatalysis,[25] CO_2 reduction,[26] CO_2 capture,[27] electromagnetic shielding,[28] water purification,[29,30] and biomedical applications[31] among many others. In addition, they can be used as transparent conducting electrodes,[32] gas sensors and biosensors.[33]

Several methods have been reported for MXenes synthesis, most of which selectively etch the Al layers from an Al-containing, parent MAX phase. A common etchant is hydrofluoric acid (HF), that results in multilayered, ML, MXenes. The latter are subsequently intercalated with polar aprotic solvents such as dimethyl sulfoxide (DMSO)[34] or organic bases, such as tetrabutylammonium hydroxide (TBAOH).[35] This step delaminates the ML's into single or few flakes after shaking or sonication.

[a]*Thin Film Physics Division, Department of Physics, Chemistry and Biology (IFM), Linköping University, SE-58183 Linköping, Sweden. E-mail: joseph.halim@liu.se, johanna.rosen@liu.se*
[b]*Plansee Composite Materials GmbH, Lechbruck, 86983 Germany*
[c]*Department of Materials Science & Engineering, Drexel University, Philadelphia, Pennsylvania 19104, USA*

†Electronic supplementary information (ESI) available. See DOI: 10.1039/d0nr07045a

Another widely used method to produce MXene single sheets, especially $Ti_3C_2T_z$, without the aid of an intercalant, involves etching of the A layer by a mixture of lithium fluoride (LiF) and hydrochloric acid (HCl) solution.[36] Other methods have been reported recently, including mixing HF with other acids, such as HNO_3,[37] using fluorine-containing organic solvents,[64] or by a reaction between the MAX phase and molten salts, such as $ZnCl_2$, where the Zn replaces the A layer and is subsequently removed using HCl.[38]

Most recently, it has been reported that the MAX phase structure and properties strongly influence the quality of the resulting MXene. In the case of $Ti_3C_2T_z$, precursors synthetized using three carbon sources (graphite, carbon lampblack and TiC) resulted in MAX phases of different purities and MXenes of different qualities and properties.[39] Hence, targeting high quality MXene starts with tailoring of MAX phase precursor.

The MAX phases can be alloyed on the M,[40,41] A[40,42] and/or X[40,43] sites, typically forming disordered solid solutions. Recently, however, chemically ordering in quaternary MAX phases has been shown for M-site alloying.[13] Two types of ordering have been demonstrated: out-of-plane (o-MAX) and in-plane (*i*-MAX). The *o*-MAX phases have n = 2 or 3, such as Mo_2TiAlC_2 and $Mo_2Ti_2AlC_2$, where Mo occupies the M-element layers closest to Al, and Ti the layers sandwiched between the carbon layers.[44] In contrast, *i*-MAX phases, with n = 1, are chemically ordered in the basal plane, such as $(Mo_{2/3}Sc_{1/3})_2AlC$, where the ratio between the two M elements is 2 : 1.[45] Unlike the conventional MAX phases with $P6_3/mmc$ symmetry, the *i*-MAX phases crystallize with in the ($C2/c$), ($C2/m$) or ($Cmcm$) symmetry, with the A-element forming a Kagomé-like lattice.[45,46] When etching the *i*-MAX phases to obtain their MXenes, the minority M-element is typically removed along with the A element, resulting in ordered vacancies.[47] For example, etching $(Mo_{2/3}Sc_{1/3})_2AlC$ results in the removal of both Sc and Al, producing a vacancy-ordered $Mo_{1.33}CT_z$ MXene.[48] To date, there has been 32 experimentally reported *i*-MAX phases, and two vacancy-ordered MXenes: $Mo_{1.33}CT_z$ and $W_{1.33}CT_z$.[24,48] Another variation on this scheme is the idea of "targeted etching", in which an *i*-MAX phase can be etched to either remove the minority M element, in addition to the A-layers, *or* not remove the former. An example of this approach is $(Mo_{2/3}Y_{1/3})_2AlC$.[49]

The introduction of vacancies, ordered or otherwise, can enhance the specific charge stored on supercapacitor electrodes and hydrogen evolution applications.[24,48,50,51] A good example is $Mo_{1.33}CT_z$, produced by etching of Al and Sc from $(Mo_{2/3}Sc_{1/3})_2AlC$. After etching, volumetric capacitances of ≈1150 F cm^{-3} before annealing[48] and 1635 F cm^{-3} after annealing in Ar[52] were obtained. The latter is the highest MXene volumetric capacitance reported to date. Fueled by these remarkable properties, several studies have been dedicated to fundamental investigations of $Mo_{1.33}CT_z$ [53,54] as well as its performance in various applications.[50,51,55]

The main drawback of the Sc-containing MAX phase is the cost and availability of Sc.[56] To address this problem, we previously synthesized the corresponding MXene starting with the Y-containing i-MAX phase, $(Mo_{2/3}Y_{1/3})_2AlC$.[49] And while the synthesis was successful, the yields and quality of the resulting MXene were low.

The purpose of this paper is to report on a new method to synthesize $(Mo_{2/3}Y_{1/3})_2AlC$ that results in higher MXene yield and quality. Instead of starting with elemental Y we started with an $AlY_{2.3}$ alloy, greatly increasing the yield. To demonstrate the quality of the resulting MXene, we fabricated supercapacitor electrodes and showed them to be as good as their counterparts made with the much rarer element, Sc.

2. Results and discussion

2.1. Synthesis and characterization of $(Mo_{2/3}Y_{1/3})_2AlC$

Synthesis of $(Mo_{2/3}Y_{1/3})_2AlC$ was carried out by mixing Mo, Al, an Al–Y 12/88 wt% alloy (corresponding to $AlY_{2.3}$), and C powders in a 1 : 0.15 : 0.53 : 0.09 mass ratio, which translates to a chemistry of $(Mo_{2/3}Y_{1/3})_2AlC$. A schematic of the *i*-MAX along the [11$\bar{2}$0] zone axis is shown in Fig. 1, (left). The powder mixture was heated in an alumina tube furnace at 1500 °C for 10 h. More details can be found in the Experimental section below. It should be noted that the $AlY_{2.3}$ used in this work is preferred from a sustainability perspective, originating from the by-product (particles of size <45 μm) obtained during the milling of $AlY_{2.3}$ ingots. The sample produced by this method will from this point forward be called $(Mo_{2/3}Y_{1/3})_2AlC$[AlY].

Fig. 2a shows the Rietveld refinement of a typical X-ray diffraction (XRD) pattern of $(Mo_{2/3}Y_{1/3})_2AlC$[AlY]. Fig. 2b shows the corresponding pattern as reported in ref. 45 in which we started with elemental powders, henceforth referred to as $(Mo_{2/3}Y_{1/3})_2AlC$[Y]. According to the Rietveld refinement (see details in ESI Tables S1 and S2†), the amount of the *i*-MAX phase increased from 45 to 75 wt% for $(Mo_{2/3}Y_{1/3})_2AlC$[AlY] compared to $(Mo_{2/3}Y_{1/3})_2AlC$[Y]. Concomitantly, the wt% of Mo_3Al_2C is reduced from 31.4% to 4.5%. It follows that starting with $AlY_{2.3}$ increased the purity of the requisite phase.

The particle morphology of the $(Mo_{2/3}Y_{1/3})_2AlC$[AlY] sample is shown in the SEM micrograph in Fig. 2c. The particle size, obtained from an average of more than 20 particles identified using SEM and EDX, is 15.5 ± 5.0 μm, which is in the same range as that obtained using the conventional synthesis method. Like in our previous work, the symmetry of crystal structure of the main phase was confirmed by both STEM (Fig. 2d and S1†) and Rietveld refinement analysis of the XRD pattern (Fig. 2a) to be monoclinic ($C2/c$). Further structural confirmation was performed by obtaining the HRSTEM images of the sample viewed in three in-plane crystallographic directions. The HRSTEM image (Fig. 2d) shows the *i*-MAX phase from the [11$\bar{2}$0] orientation, also shown in the schematic in Fig. 1. The in-plane ordering of Mo and Y is evident, with the minority element, Y, being closer to the Al-layers. The latter is rearranged into a Kagomé-like order, which causes the alternating strong/weak contrast of every second Al column.[45] HRSTEM images for two other orientations can be found in

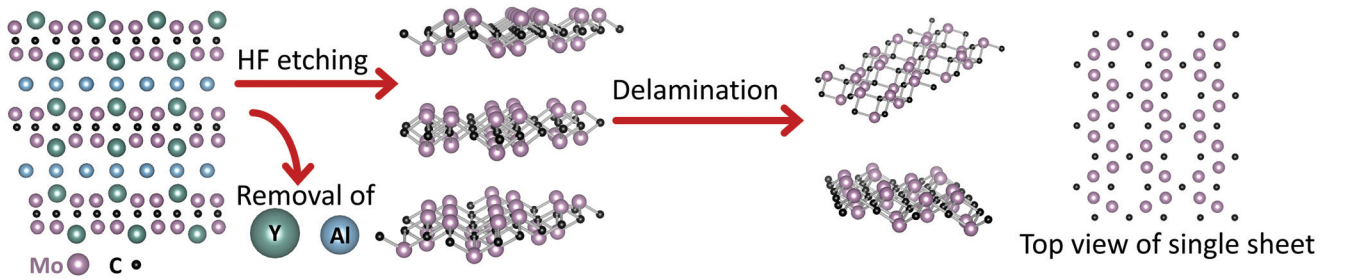

Fig. 1 Crystal structure of $(Mo_{3/2}Y_{1/3})_2AlC$ (left) along [1120]. Etching and removal of Y and Al atoms results in multilayered $Mo_{1.33}CT_z$, that is subsequently delaminated into single flakes (middle). Top view of a single flake is shown on right. Mo and C atoms are depicted by violet and black spheres, respectively.

ESI.† The lattice parameters *a*, *b*, *c* were calculated from the Rietveld refinement analysis of the XRD pattern (Fig. 2a) to be 9.54 Å, 5.52 Å and 14.07 Å, respectively. The β angle was calculated to be 103.56°, which is in agreement with our previous work (see ESI†).

2.2. Synthesis and characterization of $Mo_{1.33}CT_z$[AlY]

A schematic of the synthesis process is shown in Fig. 1, and the synthesis details are described in the Experimental section below. Immersing the parent MAX phase in HF at room temp-

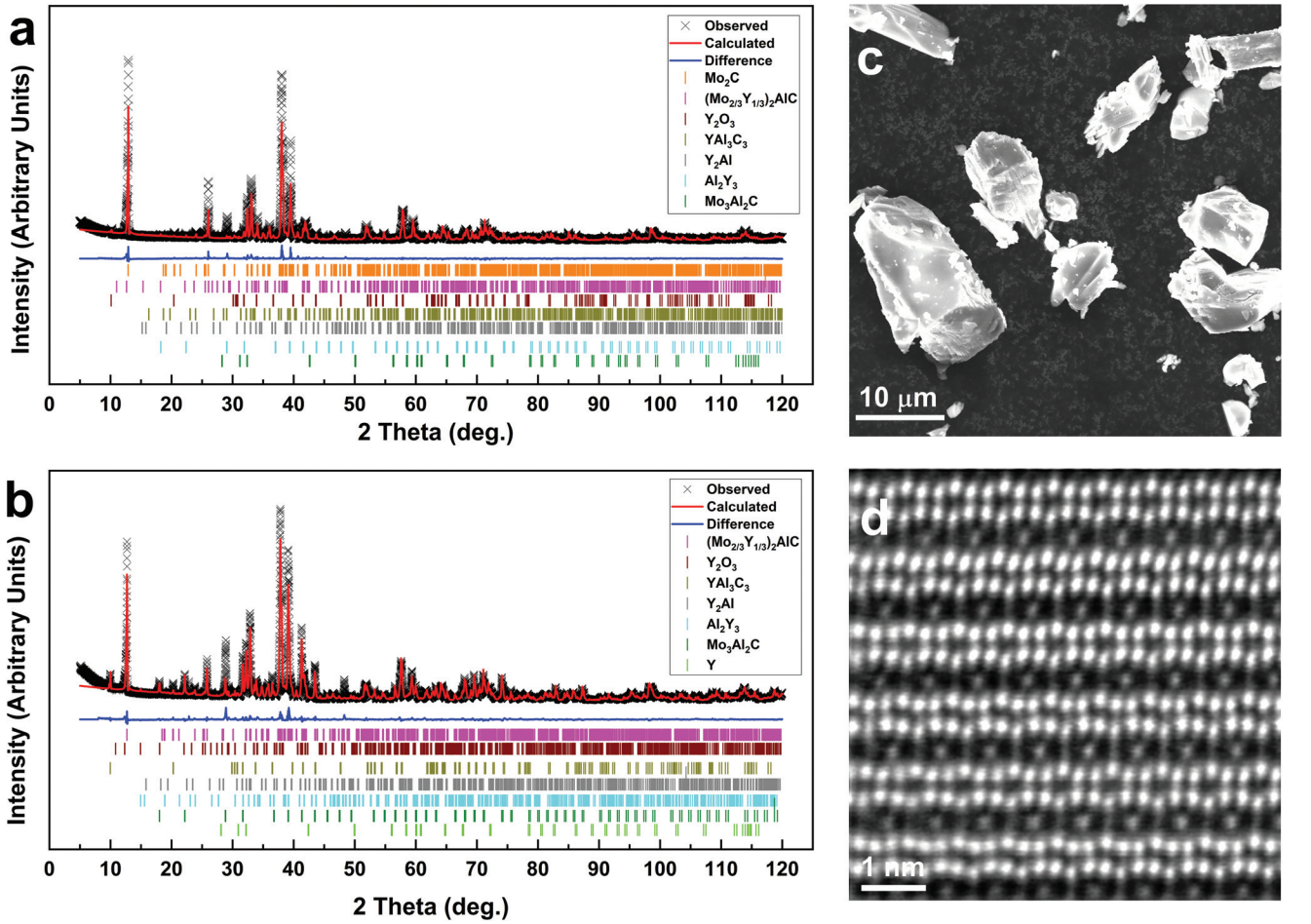

Fig. 2 (a) XRD patterns indexed to $(Mo_{2/3}Y_{1/3})_2AlC$[AlY] powder, showing measured pattern (black crosses), Rietveld generated pattern (red line) and difference between the two (blue line). The orange, pink, wine, olive, grey, light below and green ticks below the pattern represent the peak positions of Mo_2C, $(Mo_{2/3}Y_{1/3})_2AlC$, Y_2O_3, YAl_3C_3, Y_2Al, Al_2Y_3 and Mo_3Al_2C, respectively. (b) Same as (a) but for $(Mo_{2/3}Y_{1/3})_2AlC$[Y] and the pink, wine, olive, grey, light blue, green, light green ticks below the pattern represent the peak positions of $(Mo_{2/3}Y_{1/3})_2AlC$, Y_2O_3, YAl_3C_3, Y_2Al, Al_2Y_3, Mo_3Al_2C and Y, respectively. (c) SEM micrograph of typical $(Mo_{2/3}Y_{1/3})_2AlC$[AlY] particles and, (d) STEM micrograph of $(Mo_{2/3}Y_{1/3})_2AlC$[AlY] along [11$\bar{2}$0] zone axis.

erature (RT), resulted in the selective etching of Al and the vast majority of Y atoms. The resulting ML $Mo_{1.33}CT_z$ henceforth referred to as $Mo_{1.33}CT_z$[AlY], was delaminated into a suspension of single *d*-$Mo_{1.33}CT_z$[AlY] flakes that were in turn converted into free-standing films by vacuum filtration. The etching and delamination of 2 g of $(Mo_{2/3}Y_{1/3})_2AlC$[AlY] resulted in a 50 ml suspension of *d*-$Mo_{1.33}CT_z$[AlY] flakes of concentration 3 mg ml^{-1}, which is 6 times higher than the concentration obtained in our previous work. Henceforth, our previous MXene will be labelled $Mo_{1.33}CT_z$[Y].[49]

When typical XRD patterns of $(Mo_{2/3}Y_{1/3})_2AlC$[AlY] and a free-standing film of *d*-$Mo_{1.33}CT_z$(AlY) are compared (Fig. 3a), the disappearance of the (0002) peak of the *i*-MAX (lower, black) and the appearance of two (0002) peaks at lower 2-Theta for the free-standing film (upper, red), is obvious. These patterns are very typical of the MAX to MXene conversion, which results in an increase in the interlayer spacing *d*, $d = c/2$, from 7.05 Å to 8.95 (first peak), and 17.8 Å. The *d* increase from the first to the second peak, ≈8.9 Å, is most probably due to the intercalation of TBA^+ and/or water molecules between the MLs.[35,57]

The chemical formula of our free-standing film, obtained from XPS analysis (Fig. S3, Tables S3 and S4†), is $Mo_{1.33}Y_{0.05}CO_{1.1}(OH)_{0.4}F_{0.4}{\cdot}0.5H_2O_{ads}$. This formula is comparable to that of our previous work, *viz.* $Mo_{1.2}Y_{0.01}C(OH)_{0.4}F_{0.4}0.3H_2O_{ads}$.[49] In both cases, the molar sum of the terminations, *z*, is slightly less than 2 (Fig. 3b). For details of the XPS analysis, see ESI.†

Fig. 3c is a picture of our free-standing film, clearly showing a flexibility that is superior to that of $Mo_{1.33}CT_z$[Y]. We ascribe the difference to the improved quality of the MXene synthesized here. A cross-sectional SEM micrograph showing the typical morphology of free-standing MXene films, ≈7.5 μm thick, is shown in Fig. 3d.

Overview STEM images acquired from *d*-$Mo_{1.33}CT_z$[AlY] flakes (Fig. 3e and S2†) show the undulating appearance of a vacancy-ordered MXene, even more evident from the higher-magnification STEM image in Fig. 3f. These images demon-

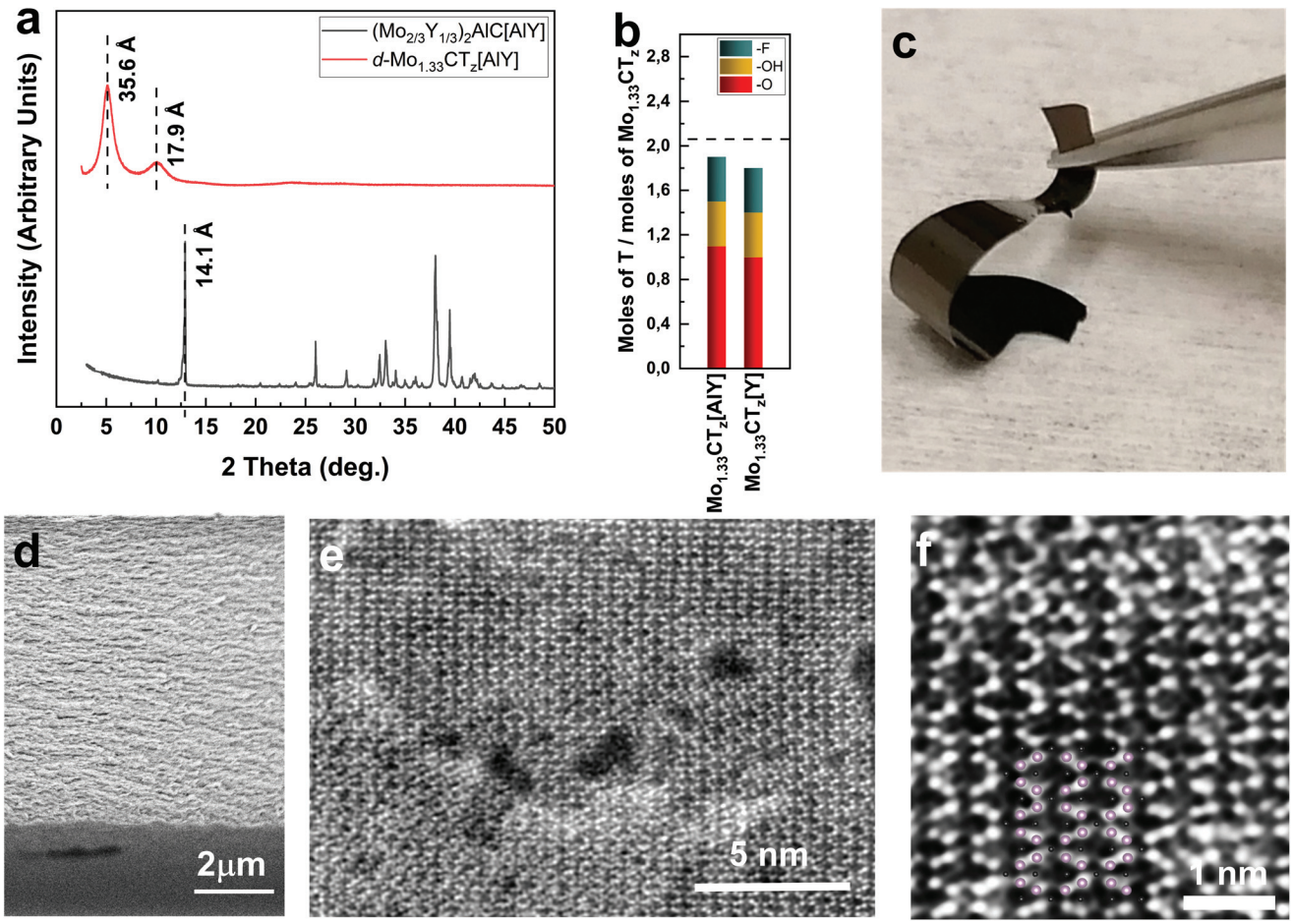

Fig. 3 (a) XRD patterns of $(Mo_{2/3}Y_{1/3})_2AlC$[AlY] (bottom, black) and *d*-$Mo_{1.33}CT_z$[AlY] free-standing films, *c* lattice parameters are shown for (0002) peaks belonging to MAX and MXene XRD patterns. (b) Moles of surface terminations T for $Mo_{1.33}CT_z$[AlY] and $Mo_{1.33}CT_z$[Y] free-standing films, per $Mo_{1.33}C$ formula unit, obtained from XPS analysis. Horizontal dashed line refers to theoretical value of *z* in T_z per formula, which is 2. (c) Picture of flexible free-standing film. (d) Cross sectional SEM micrograph of free-standing film. (e) Overview and (f) higher magnification STEM micrographs of $Mo_{1.33}CT_z$[AlY] single flakes with an overlaid crystal structure of single flake.

strate that our MXene has the same structure as the typical $Mo_{1.33}CT_z$ derived from $(Mo_{2/3}Sc_{1/3})_2AlC$ *i*-MAX,[48] labelled herein $Mo_{1.33}CT_z$[Sc]. It is important to note here that the size of the "pristine" regions – as measured by the average distance between larger pores – is larger here than in our previous work. Based on Fig. 3e, the average distance between the large pores is ≈5 nm. In our previous work that distance was closer to 2 nm. It follows that the etching procedure used herein is less aggressive.

Altogether, the results above show that we can synthesize a vacancy-ordered $Mo_{1.33}CT_z$ MXene from $(Mo_{2/3}Y_{1/3})_2AlC$, where we not only improve the sample purity of the precursor material by a modified synthesis process, but also increase the MXene yield 3 and 6 times, compared to when we started with $(Mo_{2/3}Sc_{1/3})_2AlC$ and $(Mo_{2/3}Y_{1/3})_2AlC$, respectively. This is crucial from an application perspective, allowing a retained high quality of the material while reducing the cost, both through use of more abundant elements and through reduced waste material (impurity phases).

2.3. Electrochemical performance in supercapacitors

The electrochemical behavior of the *d*-$Mo_{1.33}CT_z$[AlY] free-standing electrodes was measured in a 1 M H_2SO_4 electrolytic solution. Cyclic voltammetry and galvanostatic charge–discharge experiments were conducted using a potential window of −0.3–0.3 V (*vs.* Ag/AgCl). Fig. 4a shows the CVs of the first few cycles recorded at a scan rate of 10 mV s^{-1}. The potential (U) was swept from the open circuit potential, OCP, of about 0.15 V down to −0.3 V, and was then reversed to an upper cut-off potential of about 0.3 V. The shape of the cyclic voltammogram shows typical pseudocapacitive behavior.[58,59] In addition, the shapes of the 1st and 10th cycles were quite similar, reflecting the high reversibility of the system and the absence of parasitic side reactions. CVs at different scan rates 2, 5, 10, 20, 50, 100, 200, 500 and 1000 mV s^{-1} are shown in Fig. S6a and b.† As can be seen, the shape of the CV was not distorted even at high rates, reflecting the good rate performance of the electrodes.

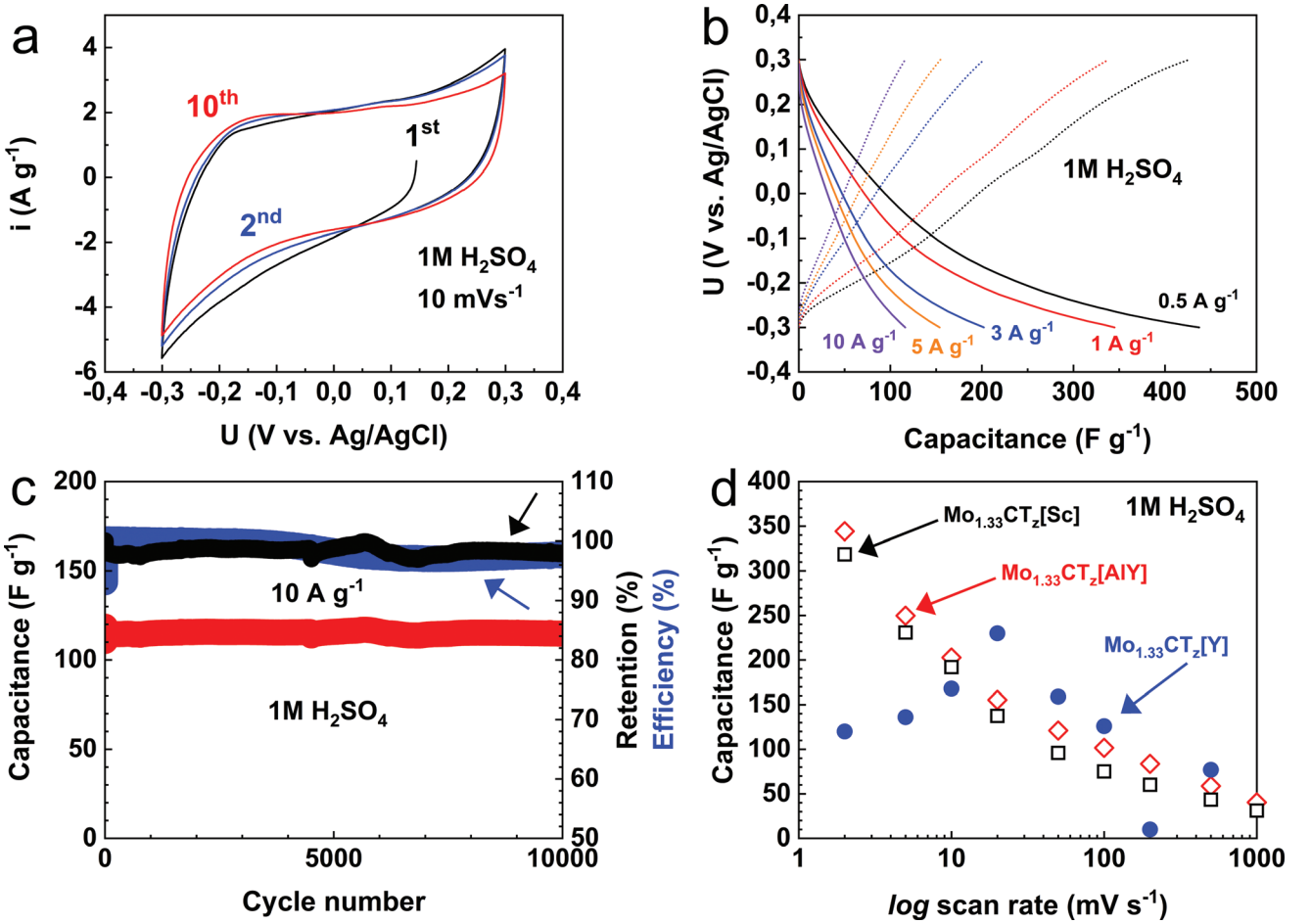

Fig. 4 Electrochemical performance of *d*-$Mo_{1.33}CT_z$[AlY] 7.5 μm thick electrodes, with a 2.1 mg cm^{-2} mass loading, in 1 M H_2SO_4 solution: (a) cyclic voltammograms at scan rates of 10 mV s^{-1}, (b) potential (U) capacitance profiles at applied current densities of 0.5 (black), 1 (red) 3 (blue), 5 (orange) and 10 (purple) A g^{-1}, (c) capacitance (red line), capacitance retention (black line) and coulombic efficiency (blue line) as a function of cycle number during long-term cycling at a current density of 10 A g^{-1}, (d) comparison of variations of gravimetric capacitance with *logarithm* of scan rates for *d*-$Mo_{1.33}CT_z$[AlY] electrodes (red diamonds), *d*-$Mo_{1.33}CT_z$[Sc] (black square), and *d*-$Mo_{1.33}CT_z$[Y] previously reported data (blue circles).[48,49]

The results of constant current measurements (Fig. 4b) were consistent with our CV results. The free-standing electrodes delivered discharge capacitances of ≈436, 345, 202, 155, and 116 F g^{-1} at current densities of 0.5, 1, 3, 5, and 10 A g^{-1}, respectively. With a measured film density of ≈3.0 g cm^{-3}, the respective volumetric capacitances are ≈1308, 1035, 606, 465, and 348 F cm^{-3}. The latter results reflect the good rate capability of the electrodes. For example, when the current density was raised by factor of 20, the capacitance retention was about 27%. Moreover, the coulombic efficiency varied between 98% to 100% at low (0.5 A g^{-1}) and high (20 A g^{-1}) current densities, respectively. One possible reason for the slightly lower coulombic efficiency at low applied current densities, can be a parasitic hydrogen evolution reaction which requires longer time to occur due to relatively slow reaction kinetics.[51]

After 10 000 cycles, at a current density of 10 A g^{-1}, 98% of the initial capacity was retained (Fig. 4c). The latter result exceeds our previously reported retentions for the *d*-$Mo_{1.33}CT_z$[Sc] and *d*-$Mo_{1.33}CT_z$[Y] films, which displayed a capacitance retentions of ≈84% (after 10 000 cycles) and 97% (after 5000 cycles), respectively.[48,49]

To probe the quality of our MXene flakes, we fabricated *d*-$Mo_{1.33}CT_z$[Sc] free-standing films (6 μm thick, density 3.5 g cm^{-3}) with the same loading as a *d*-$Mo_{1.33}CT_z$[AlY] film, 2.1 mg cm^{-2}, see the Experimental section below for the synthesis details. Fig. 4d compares the electrochemical performance of *d*-$Mo_{1.33}CT_z$[AlY] (red diamonds) and *d*-$Mo_{1.33}CT_z$[Sc] (black square) electrodes, as well as the data reported previously for *d*-$Mo_{1.33}CT_z$[Y] (blue circles).[49] As can be seen from Fig. 4d, the *d*-$Mo_{1.33}CT_z$[AlY] electrodes (morphology shown in the SEM image in Fig. S4†) reported in this study possessed the best electrochemical performance in terms of specific gravimetric capacitance as well as rate capabilities. These observations can be explained by the *d*-$Mo_{1.33}CT_z$[AlY] film being less dense than that of *d*-$Mo_{1.33}CT_z$[Sc], resulting in an increased interfacial surface accessed by the electrolyte ions (H^+) and hence an increased measured capacitance. The CVs at different scan rates for *d*-$Mo_{1.33}CT_z$[Sc] are shown in Fig. S6c and d,† while the comparison of the CVs at scanning rates 2, 10 and 1000 mV s^{-1} between *d*-$Mo_{1.33}CT_z$[AlY] and *d*-$Mo_{1.33}CT_z$[Sc] films are displayed in Fig. S7a, b and c,† respectively. The volumetric capacitance for the *d*-$Mo_{1.33}CT_z$[AlY] and *d*-$Mo_{1.33}CT_z$[Sc] films (see Fig. S4†) displayed a trend comparable to that for the gravimetric capacitance, with the exception of the low rate performance; there the volumetric capacitance of *d*-$Mo_{1.33}CT_z$[Sc] was higher than *d*-$Mo_{1.33}CT_z$[AlY], owing to the different densities of the films.

The electrochemical performance of the *d*-$Mo_{1.33}CT_z$[AlY] electrodes was further improved by using a 3 M H_2SO_4 electrolytic solution (see Fig. S8†). The *d*-$Mo_{1.33}CT_z$[AlY] electrodes delivered discharge capacitance of about 245, 200, 153, 127, and 47 F g^{-1} at current densities of 3, 5, 10, 20, and 100 A g^{-1}, respectively. With a measured density of ≈3.0 g cm^{-3}, the respective volumetric capacitances were ≈735, 600, 460, 381, and 141 F cm^{-3}. After 40 000 cycles, at a current density of 20 A g^{-1}, 98% of the initial capacity was retained (Fig. S5†). This improvement can be attributed to the increased ionic conductivity; however, the coulombic efficiency at low rate was decreased, possibly due to the increased probability for hydrogen evolution. Consequently, 3 M H_2SO_4 can be used as the electrolyte in high rate applications and 1 M H_2SO_4 can be used as the electrolyte in low rate applications.

3. Conclusions

By starting with $AlY_{2.3}$, instead of elemental Y and Al powders, we synthesized the *i*-MAX phase $(Mo_{2/3}Y_{1/3})_2AlC$. The sample was ≈75 wt% phase pure through the suppression of the formation of the major secondary phase, Mo_3Al_2C. Synthesis of vacancy-ordered $Mo_{1.33}CT_z$ i-MXene was realized through an optimized etching procedure that included etching in HF and delamination using TBAOH. The obtained MXene yield was 6 times higher compared to our previous reports wherein we started with elemental Y and Al powders. Furthermore, high resolution microscopy demonstrated sheets of high structural quality, including comparatively few and smaller pores from the etching procedure. Free-standing films showed an electrochemical performance at the level of, or beyond, previously results for $Mo_{1.33}CT_z$ derived from either $(Mo_{2/3}Y_{1/3})_2AlC$ or $(Mo_{2/3}Sc_{1/3})_2AlC$. In particular, the herein synthesized $Mo_{1.33}CT_z$ MXene electrodes tested in 1 M H_2SO_4 delivered high capacitances of about 436 F g^{-1} (1308 F cm^{-3}) and 116 F g^{-1} (348 F cm^{-3}) at low (0.5 A g^{-1}) and high (10 A g^{-1}) current densities, respectively. The rate capability of the MXene electrodes was further improved upon changing of the electrolyte to 3 M H_2SO_4. The long-term cycling showed a stable behavior with a capacity retention of 98% after 10 000 cycles.

The results presented here open the door for using $(Mo_{2/3}Y_{1/3})_2AlC$, instead of $(Mo_{2/3}Sc_{1/3})_2AlC$, to produce vacancy-ordered $Mo_{1.33}CT_z$ MXene with matching or even improved yield, quality, and performance. The importance of these findings can be expressed in terms of reduced waste material, lowered cost, use of more abundant elements, and higher applicability.

4. Experimental section

4.1. Synthesis of $(Mo_{3/2}Y_{1/3})_2AlC$[AlY]

This phase was synthetized by a solid state reaction between Mo (−3 to 7 μm, Alfa Aesar, Kandel, Germany, 99.999 wt% purity), YAl 88/12 wt% (−350 mesh, Plansee Composite Materials, Lechbruck, Germany, 99.4 wt% purity), Al (−325 mesh, Alfa Aesar, Kandel, Germany, 99.5 wt% purity), and graphite (−200 mesh, Alfa Aesar, Karlsruhe, Germany, 99.9995 wt% purity) in the molar ratio of 1.33 : 1 : 2.45 : 1, respectively, corresponding to a stoichiometry of $(Mo_{3/2}Y_{1/3})_2AlC$. These powders were manually mixed in an agate mortar, then cold pressed into 0.5 cm diameter and 1 cm thick disks using a manual hydraulic press to a load corresponding to a pressure of 70 kPa. Afterwards, the cold pressed samples were placed in an alumina crucible and

inserted in a horizontal tube furnace. The furnace was heated, under a 5 sccm Ar flow, at 5 °C min^{-1} to 1500 °C and were held at that temperature for 10 h. After furnace cooling, the samples were crushed, again, using a mortar and pestle and sieved through a 450-mesh sieve. The $(Mo_{3/2}Y_{1/3})_2AlC$[Y] and $(Mo_{2/3}Sc)_2AlC$ i-MAX powders were synthetized using the methods described previously in ref. 49 and 45, respectively.

4.2. Synthesis of $Mo_{1.33}CT_z$[AlY]

Two grams of $(Mo_{2/3}Y_{1/3})_2AlC$[AlY] powders (−450 mesh) were immersed in a Teflon bottle containing 40 ml of 25 vol% HF (Sigma Aldrich, St Louis, USA). The mixture was stirred using a Teflon coated magnetic stirrer bar for 120 h at RT. The resulting mixture was washed with N_2 deaerated deionized water (DI) for several cycles till the pH was ≈6 (typically, 8 cycles were needed). In each washing cycle, 40 ml of DI water were added to the ML powder in a centrifuge tube, and was hand-shaken for 1 min, then centrifuged at 5000 rpm for 1 min, and after that the supernatant was decanted.

For delamination, 1 g of the ML powder was added to 5 ml of an aqueous solution of 54–56 wt% TBAOH (Sigma Aldrich, Sweden). The mixture was hand-shaken for 5 min, and then washed 3 times by 40 ml deaerated DI water each time. Subsequently, 50 ml of deaerated DI water was added to the intercalated powder and hand-shaken for 5 min, followed by centrifugation at 2500 rpm for 30 min. The resultant supernatant, containing delaminated single or few layer $Mo_{1.33}CT_z$[AlY] flakes at a concentration of 3 mg ml^{-1}, was vacuum-filtered onto a nanoporous polypropylene membrane (3501 Coated PP, 0.064 μm pore size, Celgard, LLC, USA) forming a flexible free-standing film. The *d*-$Mo_{1.33}CT_z$[Sc] free-standing film was synthetized using the method described previously in ref. 45.

4.3. Materials characterization

The microstructures and morphologies of $(Mo_{2/3}Y_{1/3})_2AlC$[AlY] powder and a *d*-$Mo_{1.33}CT_z$[AlY] free-standing film were characterized using a SEM (LEO 1550 Gemini) operated with an acceleration voltage between 5 and 15 keV.

Further imaging of $(Mo_{2/3}Y_{1/3})_2AlC$[AlY] i-MAX particles and single flakes of *d*-$Mo_{1.33}CT_z$[AlY] MXene was performed using a STEM combined with high angle annular dark field imaging in a double-corrected Linköping FEI Titan^3 60–300, operated at 300 kV. A Cu grid, supporting amorphous carbon films, was used to prepare the i-MAX TEM sample by drop casting a DI water suspension containing i-MAX particles on the Cu grid. In the case of the *d*-$Mo_{1.33}CT_z$[AlY] MXene, TEM sample, the MXene colloidal suspension was drop cast onto a Cu grid. To reduce noise, combined Wiener and ABSF filtering of the HRSTEM images was applied using the HRTEM filter plugin for Digital Micrograph.[60]

X-Ray diffraction patterns for the i-MAX phase samples and free-standing *d*-$Mo_{1.33}CT_z$[AlY] films were obtained using a PANalytical X'Pert powder diffractometer with a Cu source ($\lambda_{K\alpha}$ ≈ 1.54 Å). A graded Bragg–Brentano HD, with a 1/4° divergent and 1/2° anti-scatter slits was used in the incident beam side, and a 5 mm anti-scatter slit with a Soller slit (with an opening of 0.04 radian) was used in the diffracted beam side. A continuous scan with step size of 0.008° with a 40 s time per step was performed on the samples.

The XRD patterns of the $(Mo_{2/3}Y_{1/3})_2AlC$[AlY] and $(Mo_{2/3}Y_{1/3})_2AlC$[Y] powders were analyzed by the Rietveld refinement method, using the *FULLPROF* code.[61,62] Refined parameters were the scale factors, from which the relative phase fractions were evaluated, *X* and *Y* profile parameters for peak width, lattice parameters (LPs) and atomic positions for all phases. The background was refined *via* a 6-coefficient polynomial function.

XPS measurements of the *d*-$Mo_{1.33}CT_z$[AlY] free-standing film were carried out using a surface analysis system (Kratos AXIS Ultra^{DLD}, Manchester, U.K.) with monochromatic Al-Kα X-ray (1486.6 eV) radiation. The sample was mounted on a double-sided tape and grounded to the sample stage with copper contacts. The X-ray beam irradiated the sample surface at an angle of 45°, with respect to the surface and provided an X-ray spot of ≈300 × 800 μm. Charge neutralization was performed using a co-axial, low energy (~0.1 eV) electron flood source to avoid shifts in the recorded binding energy (BE). XPS spectra were recorded for F 1s, O 1s, C 1s, Al 2p, Mo 3d and Y 3d. The analyzer pass energy used for all the regions was 20 eV with a step size of 0.1 eV. The BE scale of all XPS spectra was referenced to the Fermi-edge (E_F), which was set to a BE of zero eV. The peak fitting was carried out using CasaXPS Version 2.3.16 RP 1.6 in the same manner as in ref. 57 and 63. The global elemental percentage was quantified as in ref. 57 and 63.

4.4. Electrochemical characterization

Cyclic voltammetry and constant-current (galvanostatic charge–discharge) techniques were used to explore the electrochemical performance of the *d*-$Mo_{1.33}CT_z$ free-standing electrodes using a potential window of −0.3–0.3 V *vs.* Ag/AgCl. The electrochemical experiments were carried out using three-electrode stainless-steel Swagelok cells. The as-prepared $Mo_{1.33}CT_z$ free-standing film with a mass loading 2.1 mg cm^{-2} was punched into circular electrodes 4 mm in diameter. The electrode mass was about 250–280 μg. These electrodes were used as the working electrodes. A circular electrode of activated carbon (YP-50, Kuraray, Japan) and Ag/AgCl (saturated KCl) were used as the counter and reference electrodes, respectively. A gold foil was used as the current collector and a piece of Celgard 3501 soaked in 1 M H_2SO_4 solution (500 μl) was used as a separator.

Additional experiments were performed using a 3 M H_2SO_4 solution. For volumetric capacitance calculations, the density of the MXene film was deduced from the film thickness and its mass was found to be 2.8–3.0 g cm^{-3}.

The charge/discharge capacitance (F g^{-1}) was determined by integrating the anodic/cathodic charge portions in the cyclic voltammograms using the relation:

$$\text{Gravimetric capacitance}(\text{F g}^{-1}) = \frac{1}{V \times m \times \nu}\int i\mathrm{d}V$$

where V: is the potential window (V), m: is the mass of active material (g), v: is the scan rate (V s^{-1}), and i: is the charging/discharging current (A).

$$\text{Volumetric capacitance}(\text{F cm}^{-3}) = \text{gravimetric capacitance}(\text{F g}^{-1})\text{packing density}(\text{g cm}^{-3})$$

Conflicts of interest

There are no conflicts to declare.

Acknowledgements

J. R. acknowledges support from the Knut and Alice Wallenberg (KAW) Foundation for a Fellowship/Scholar Grant, and from the Swedish Foundation for Strategic Research (SSF) for Project Funding (EM16-0004). The KAW Foundation is also acknowledged for support to the Linköping Electron Microscopy Laboratory. P. Å. O. P. acknowledges the Swedish Research Council for funding under grant no. 2016–04412, Swedish Foundation for Strategic Research (SSF) through the Research Infrastructure Fellow program no. RIF 14-0074, and the Swedish Government Strategic Research Area in Materials Science on Functional Materials at Linköping University (Faculty Grant SFO-Mat-LiU no. 2009 00971).

References

1 R. Mas-Balleste, C. Gomez-Navarro, J. Gomez-Herrero and F. Zamora, *Nanoscale*, 2011, **3**, 20–30.
2 X. Chia and M. Pumera, *Nat. Catal.*, 2018, **1**, 909–921.
3 Y. Chen, Z. Fan, Z. Zhang, W. Niu, C. Li, N. Yang, B. Chen and H. Zhang, *Chem. Rev.*, 2018, **118**, 6409–6455.
4 K. S. Kumar, N. Choudhary, Y. Jung and J. Thomas, *ACS Energy Lett.*, 2018, **3**, 482–495.
5 W. Lee, Y. Liu, Y. Lee, B. K. Sharma, S. M. Shinde, S. D. Kim, K. Nan, Z. Yan, M. Han and Y. Huang, *Nat. Commun.*, 2018, **9**, 1–9.
6 M. W. Barsoum, *MAX phases: properties of machinable ternary carbides and nitrides*, John Wiley & Sons, 2013.
7 M. Naguib, M. Kurtoglu, V. Presser, J. Lu, J. Niu, M. Heon, L. Hultman, Y. Gogotsi and M. W. Barsoum, *Adv. Mater.*, 2011, **23**, 4248–4253.
8 M. Naguib, O. Mashtalir, J. Carle, V. Presser, J. Lu, L. Hultman, Y. Gogotsi and M. W. Barsoum, *ACS Nano*, 2012, **6**, 1322–1331.
9 T. H. Scabarozi, S. Amini, P. Finkel, O. D. Leaffer, J. E. Spanier, M. W. Barsoum, M. Drulis, H. Drulis, W. M. Tambussi and J. D. Hettinger, *J. Appl. Phys.*, 2008, **104**, 33502.
10 J. D. Hettinger, S. E. Lofland, P. Finkel, T. Meehan, J. Palma, K. Harrell, S. Gupta, A. Ganguly, T. El-Raghy and M. W. Barsoum, *Phys. Rev. B: Condens. Matter Mater. Phys.*, 2005, **72**, 115120.
11 M. W. Barsoum and M. Radovic, *Annu. Rev. Mater. Res.*, 2011, **41**, 195–227.
12 M. W. Barsoum and T. El-Raghy, *Am. Sci.*, 2001, **89**, 334–343.
13 M. Sokol, V. Natu, S. Kota and M. W. Barsoum, *Trends Chem.*, 2019, **1**, 210–223.
14 A. S. Ingason, M. Dahlqvist and J. Rosén, *J. Phys.: Condens. Matter*, 2016, **28**, 433003.
15 M. Naguib, V. N. Mochalin, M. W. Barsoum and Y. Gogotsi, *Adv. Mater.*, 2014, **26**, 992–1005.
16 J. Halim, K. M. Cook, P. Eklund, J. Rosen and M. W. Barsoum, *Appl. Surf. Sci.*, 2019, **494**, 1138–1147.
17 M. A. Hope, A. C. Forse, K. J. Griffith, M. R. Lukatskaya, M. Ghidiu, Y. Gogotsi and C. P. Grey, *Phys. Chem. Chem. Phys.*, 2016, **18**, 5099–5102.
18 T. Kobayashi, Y. Sun, K. E. Prenger, D.-E. Jiang, M. Naguib and M. Pruski, *J. Phys. Chem. C*, 2020, **124**, 13649–13655.
19 J. Lu, I. Persson, H. Lind, J. Palisaitis, M. Li, Y. Li, K. Chen, J. Zhou, S. Du and Z. Chai, *Nanoscale Adv.*, 2019, **1**, 3680–3685.
20 B. Anasori, M. R. Lukatskaya and Y. Gogotsi, *Nat. Rev. Mater.*, 2017, **2**, 1–17.
21 K. R. G. Lim, A. D. Handoko, S. K. Nemani, B. Wyatt, H.-Y. Jiang, J. Tang, B. Anasori and Z. W. Seh, *ACS Nano*, 2020, **14**, 10834–10864.
22 Z. W. Seh, K. D. Fredrickson, B. Anasori, J. Kibsgaard, A. L. Strickler, M. R. Lukatskaya, Y. Gogotsi, T. F. Jaramillo and A. Vojvodic, *ACS Energy Lett.*, 2016, **1**, 589–594.
23 A. D. Handoko, K. D. Fredrickson, B. Anasori, K. W. Convey, L. R. Johnson, Y. Gogotsi, A. Vojvodic and Z. W. Seh, *ACS Appl. Energy Mater.*, 2017, **1**, 173–180.
24 R. Meshkian, M. Dahlqvist, J. Lu, B. Wickman, J. Halim, J. Thörnberg, Q. Tao, S. Li, S. Intikhab and J. Snyder, *Adv. Mater.*, 2018, **30**, 1706409.
25 T. Su, R. Peng, Z. D. Hood, M. Naguib, I. N. Ivanov, J. K. Keum, Z. Qin, Z. Guo and Z. Wu, *ChemSusChem*, 2018, **11**, 688–699.
26 A. D. Handoko, H. Chen, Y. Lum, Q. Zhang, B. Anasori and Z. W. Seh, *iScience*, 2020, **23**, 101181.
27 I. Persson, J. Halim, H. Lind, T. W. Hansen, J. B. Wagner, L. Näslund, V. Darakchieva, J. Palisaitis, J. Rosen and P. O. Å. Persson, *Adv. Mater.*, 2019, **31**, 1805472.
28 F. Shahzad, M. Alhabeb, C. B. Hatter, B. Anasori, S. M. Hong, C. M. Koo and Y. Gogotsi, *Science*, 2016, **353**, 1137–1140.
29 P. Srimuk, J. Halim, J. Lee, Q. Tao, J. Rosen and V. Presser, *ACS Sustainable Chem. Eng.*, 2018, **6**, 3739–3747.
30 X. Xie, C. Chen, N. Zhang, Z.-R. Tang, J. Jiang and Y.-J. Xu, *Nat. Sustainability*, 2019, **2**, 856–862.
31 K. Huang, Z. Li, J. Lin, G. Han and P. Huang, *Chem. Soc. Rev.*, 2018, **47**, 5109–5124.
32 J. Halim, M. R. Lukatskaya, K. M. Cook, J. Lu, C. R. Smith, L.-Å. Näslund, S. J. May, L. Hultman, Y. Gogotsi and P. Eklund, *Chem. Mater.*, 2014, **26**, 2374–2381.
33 A. Sinha, H. Zhao, Y. Huang, X. Lu, J. Chen and R. Jain, *TrAC, Trends Anal. Chem.*, 2018, **105**, 424–435.

34 O. Mashtalir, M. Naguib, V. N. Mochalin, Y. Dall’ Agnese, M. Heon, M. W. Barsoum and Y. Gogotsi, *Nat. Commun.*, 2013, **4**, 1–7.
35 M. Naguib, R. R. Unocic, B. L. Armstrong and J. Nanda, *Dalton Trans.*, 2015, **44**, 9353–9358.
36 M. Ghidiu, M. R. Lukatskaya, M.-Q. Zhao, Y. Gogotsi and M. W. Barsoum, *Nature*, 2014, **516**, 78–81.
37 M. Alhabeb, K. Maleski, T. S. S. Mathis, A. Sarycheva, C. B. B. Hatter, S. Uzun, A. Levitt and Y. Gogotsi, *Angew. Chem., Int. Ed.*, 2018, **57**, 5444–5448.
38 M. Li, J. Lu, K. Luo, Y. Li, K. Chang, K. Chen, J. Zhou, J. Rosen, L. Hultman and P. Eklund, *J. Am. Chem. Soc.*, 2019, **141**, 4730–4737.
39 C. E. Shuck, M. Han, K. Maleski, K. Hantanasirisakul, S. J. Kim, J. Choi, W. E. B. Reil and Y. Gogotsi, *ACS Appl. Nano Mater.*, 2019, **2**, 3368–3376.
40 M. A. Pietzka and J. C. Schuster, *Phase Equilib.*, 1994, **15**, 392.
41 M. Naguib, G. W. Bentzel, J. Shah, J. Halim, E. N. Caspi, J. Lu, L. Hultman and M. W. Barsoum, *Mater. Res. Lett.*, 2014, **2**, 233–240.
42 X. Xu, T. L. Ngai and Y. Li, *Ceram. Int.*, 2015, **41**, 7626–7631.
43 B. Manoun, S. K. Saxena, G. Hug, A. Ganguly, E. N. Hoffman and M. W. Barsoum, *J. Appl. Phys.*, 2007, **101**, 113523.
44 B. Anasori, M. Dahlqvist, J. Halim, E. J. Moon, J. Lu, B. C. Hosler, E. N. Caspi, S. J. May, L. Hultman and P. Eklund, *J. Appl. Phys.*, 2015, **118**, 94304.
45 M. Dahlqvist, J. Lu, R. Meshkian, Q. Tao, L. Hultman and J. Rosen, *Sci. Adv.*, 2017, **3**, e1700642.
46 Q. Tao, J. Lu, M. Dahlqvist, A. Mockute, S. Calder, A. Petruhins, R. Meshkian, O. Rivin, D. Potashnikov and E. N. Caspi, *Chem. Mater.*, 2019, **31**, 2476–2485.
47 P. O. Å. Persson and J. Rosen, *Curr. Opin. Solid State Mater. Sci.*, 2019, **23**, 100774.
48 Q. Tao, M. Dahlqvist, J. Lu, S. Kota, R. Meshkian, J. Halim, J. Palisaitis, L. Hultman, M. W. Barsoum, P. O. Å. Persson and J. Rosen, *Nat. Commun.*, 2017, **8**, 14949.
49 I. Persson, A. El Ghazaly, Q. Tao, J. Halim, S. Kota, V. Darakchieva, J. Palisaitis, M. W. Barsoum, J. Rosen and P. O. Å. Persson, *Small*, 2018, **14**, 1703676.
50 L. Qin, Q. Tao, A. El Ghazaly, J. Fernandez-Rodriguez, P. O. Å. Persson, J. Rosen and F. Zhang, *Adv. Funct. Mater.*, 2018, **28**, 1703808.
51 S. Intikhab, V. Natu, J. Li, Y. Li, Q. Tao, J. Rosen, M. W. Barsoum and J. Snyder, *J. Catal.*, 2019, **371**, 325–332.
52 B. Ahmed, A. El Ghazaly and J. Rosen, *Adv. Funct. Mater.*, 2020, 2000894.
53 H. Lind, J. Halim, S. I. Simak and J. Rosén, *Phys. Rev. Mater.*, 2017, **1**, 44002.
54 J. Halim, E. J. Moon, P. Eklund, J. Rosen, M. W. Barsoum and T. Ouisse, *Phys. Rev. B*, 2018, **98**, 104202.
55 Y. Liu, Q. Tao, Y. Jin, X. Liu, H. Sun, A. El Ghazaly, S. Fabiano, Z. Li, J. Luo and J. Rosen, *ACS Appl. Electron. Mater.*, 2019, **2**, 163–169.
56 C. T. Horovitz, *Scandium its occurrence, chemistry physics, metallurgy, biology and technology*, Elsevier, 2012.
57 J. Halim, S. Kota, M. R. Lukatskaya, M. Naguib, M. Zhao, E. J. Moon, J. Pitock, J. Nanda, S. J. May and Y. Gogotsi, *Adv. Funct. Mater.*, 2016, **26**, 3118–3127.
58 T. S. Mathis, N. Kurra, X. Wang, D. Pinto, P. Simon and Y. Gogotsi, *Adv. Energy Mater.*, 2019, **9**, 1902007.
59 B. E. Conway, in *Electrochemical Supercapacitors*, Springer, 1999, pp. 1–9.
60 D. R. G. Mitchell, 2019, http://www.dmscripting.com/hrtem_filter.html.
61 H. Rietveld, *J. Appl. Crystallogr.*, 1969, **2**, 65–71.
62 J. Rodríguez-Carvajal, *Phys. B*, 1993, **192**, 55–69.
63 J. Halim, K. M. Cook, M. Naguib, P. Eklund, Y. Gogotsi, J. Rosen and M. W. Barsoum, *Appl. Surf. Sci.*, 2016, **362**, 406–417.
64 V. Natu, *Chem*, 2020, **6**(3), 616–630.